PLASMA ASTROPHYSICS

Electron-scale dynamics of the diffusion region during symmetric magnetic reconnection in space

R. B. Torbert[1,2]*, J. L. Burch[2], T. D. Phan[3], M. Hesse[2,4], M. R. Argall[1], J. Shuster[5], R. E. Ergun[6], L. Alm[7], R. Nakamura[8], K. J. Genestreti[8], D. J. Gershman[5], W. R. Paterson[5], D. L. Turner[9], I. Cohen[10], B. L. Giles[5], C. J. Pollock[5], S. Wang[11], L.-J. Chen[5,11], J. E. Stawarz[12], J. P. Eastwood[12], K. J. Hwang[2], C. Farrugia[1], I. Dors[1], H. Vaith[1], C. Mouikis[1], A. Ardakani[1], B. H. Mauk[10], S. A. Fuselier[2,13], C. T. Russell[14], R. J. Strangeway[14], T. E. Moore[5], J. F. Drake[11], M. A. Shay[15], Yuri V. Khotyaintsev[7], P.-A. Lindqvist[16], W. Baumjohann[8], F. D. Wilder[6], N. Ahmadi[6], J. C. Dorelli[5], L. A. Avanov[5], M. Oka[3], D. N. Baker[6], J. F. Fennell[9], J. B. Blake[9], A. N. Jaynes[17], O. Le Contel[18], S. M. Petrinec[19], B. Lavraud[20], Y. Saito[21]

Magnetic reconnection is an energy conversion process that occurs in many astrophysical contexts including Earth's magnetosphere, where the process can be investigated in situ by spacecraft. On 11 July 2017, the four Magnetospheric Multiscale spacecraft encountered a reconnection site in Earth's magnetotail, where reconnection involves symmetric inflow conditions. The electron-scale plasma measurements revealed (i) super-Alfvénic electron jets reaching 15,000 kilometers per second; (ii) electron meandering motion and acceleration by the electric field, producing multiple crescent-shaped structures in the velocity distributions; and (iii) the spatial dimensions of the electron diffusion region with an aspect ratio of 0.1 to 0.2, consistent with fast reconnection. The well-structured multiple layers of electron populations indicate that the dominant electron dynamics are mostly laminar, despite the presence of turbulence near the reconnection site.

Magnetic reconnection, a large-scale plasma process that converts electromagnetic energy to particle energy, is the dominant mechanism by which solar wind energy enters Earth's magnetosphere. This energy is subsequently dissipated by geomagnetic substorms and aurorae (*1*, *2*). Although the consequences of reconnection are large-scale, the process starts at the small ion scale, and even smaller, the electron-scale diffusion region (EDR). Studying the physical processes that cause magnetic reconnection requires determining structures and dynamics inside the EDR with sufficiently high-resolution plasma and field measurements (*3*), beyond the capabilities of previous spacecraft missions that have encountered the EDR (*4*–*6*).

The Magnetospheric Multiscale (MMS) mission focuses on investigating two reconnection regions known to exist around Earth: the dayside magnetopause and the nightside magnetotail, which host very different plasma parameter regimes. During its first phase (2015–2016), the four MMS spacecraft investigated reconnection in the dayside magnetopause (*3*), where the inflow conditions are highly asymmetric, with different plasma and magnetic pressures in the two inflow regions. In dayside reconnection, magnetic energy conversion processes occur in two separated regions: the X-line, where the magnetic field reverses, and the electron flow stagnation point (*7*, *8*). In its second phase (2017), MMS explored the kinetic processes of reconnection in Earth's magnetotail where the inflow conditions are nearly symmetric, the available magnetic energy per particle is more than an order of magnitude higher than on the dayside, and the X-line and stagnation point are coincident (*9*). The amount of magnetic energy per particle in the magnetotail is comparable to that of the solar corona, where magnetic reconnection also occurs.

On 11 July 2017 at ~22:34 Universal Time (UT), MMS encountered an EDR when it detected tailward-directed ion and electron jets (negative ion and electron bulk velocities, V_{iL} and V_{eL}; Fig. 1, F and G) followed by earthward-directed jets, spanning a reversal of essentially the north-south component of the magnetotail magnetic field B_N (Fig. 1D) in an intense current sheet (large out-of-plane electron velocity V_{eM}). We adopt an *LMN* coordinate system to orient the data to the usual 2D view of the magnetic field near a reconnection X-line (Fig. 1J), with L in the outflow direction, M along the X-line, and N normal to the current sheet (*10*). The out-of-plane guide field ratio, B_M/B_L, for this event is estimated to be small (<10%) (*10*). The spacecraft were in the magnetotail at a radial distance from Earth of 22 Earth radii. Four-spacecraft timing of the flow and field reversals indicate that the structure moved away from Earth with velocity V_L ~ −170 km/s. These are signatures of a tailward retreat of the reconnection X-line past the spacecraft, as indicated by the MMS path in Fig. 1J (*5*, *6*, *11*–*16*). Except for a brief excursion to the edge of the inflow region, seen in a small perturbation in magnetic field components beginning at 22:34:00 UT (due to a flapping of the current sheet), the spacecraft stayed close to the neutral sheet (B_L = 0 plane), indicated by small values of $|B_L|$ (~0 to 2 nT), during the flow and field reversal. These observations are consistent with crossing both ion and electron diffusion regions—an identification that is supported by the profiles of the ion and electron flows: V_{eM} peaked at ~ −15,000 km/s, within an order of magnitude of the electron Alfvén speed $B/\sqrt{2\mu_0 m_e n_e}$ (where m_e and n_e are electron mass and density), approximately 20,000 to 25,000 km/s. Starting from the X-line (at the $\mathbf{V}_{eL}$ and $\mathbf{B}$ reversal location) and going left and right in Fig. 1H, the electron perpendicular outflow speed $|V_{e\perp L}|$ increased and greatly exceeded the ion speed. While the ion outflow speed ($|V_{iL}|$; Fig. 1F) increased with increasing distance from the X-line, $|V_{e\perp L}|$ reached a peak (~7000 km/s) before slowing and approaching the ion flow speed at ~22:33:50 before, and ~22:34:20 after, the X-line. Thus, the ends of the ion diffusion region, where the ion and electron outflow velocities are expected to match, are likely encountered near these times. The end of the electron diffusion region, on the other hand, marked by the departure of $V_{e\perp}$ from $\mathbf{E} \times \mathbf{B}/B^2$, was confined to a much smaller interval around the X-line, where the electron density reached a symmetric minimum of 0.03 cm^{-3} (electron inertial length d_e ~ 30 km).

[1]University of New Hampshire, Durham, NH, USA. [2]Southwest Research Institute (SwRI), San Antonio, TX, USA. [3]University of California, Berkeley, CA, USA. [4]University of Bergen, Bergen, Norway. [5]NASA Goddard Space Flight Center, Greenbelt, MD, USA. [6]University of Colorado Laboratory for Atmospheric and Space Physics, Boulder, CO, USA. [7]Swedish Institute of Space Physics, Uppsala, Sweden. [8]Space Research Institute, Austrian Academy of Sciences, Graz, Austria. [9]Aerospace Corporation, El Segundo, CA, USA. [10]Johns Hopkins University Applied Physics Laboratory, Laurel, MD, USA. [11]University of Maryland, College Park, MD, USA. [12]Blackett Laboratory, Imperial College London, London, UK. [13]University of Texas, San Antonio, TX, USA. [14]University of California, Los Angeles, CA, USA. [15]University of Delaware, Newark, DE, USA. [16]Royal Institute of Technology, Stockholm, Sweden. [17]University of Iowa, Iowa City, IA, USA. [18]Laboratoire de Physique des Plasmas, CNRS/Ecole Polytechnique/Sorbonne Université/Univ. Paris Sud/Observatoire de Paris, Paris, France. [19]Lockheed Martin Advanced Technology Center, Palo Alto, CA, USA. [20]Institut de Recherche en Astrophysique et Planétologie, CNRS, Centre National d'Etudes Spatiales, Université de Toulouse, Toulouse, France. [21]Institute for Space and Astronautical Sciences, Sagamihara, Japan.
*Corresponding author. Email: roy.torbert@unh.edu

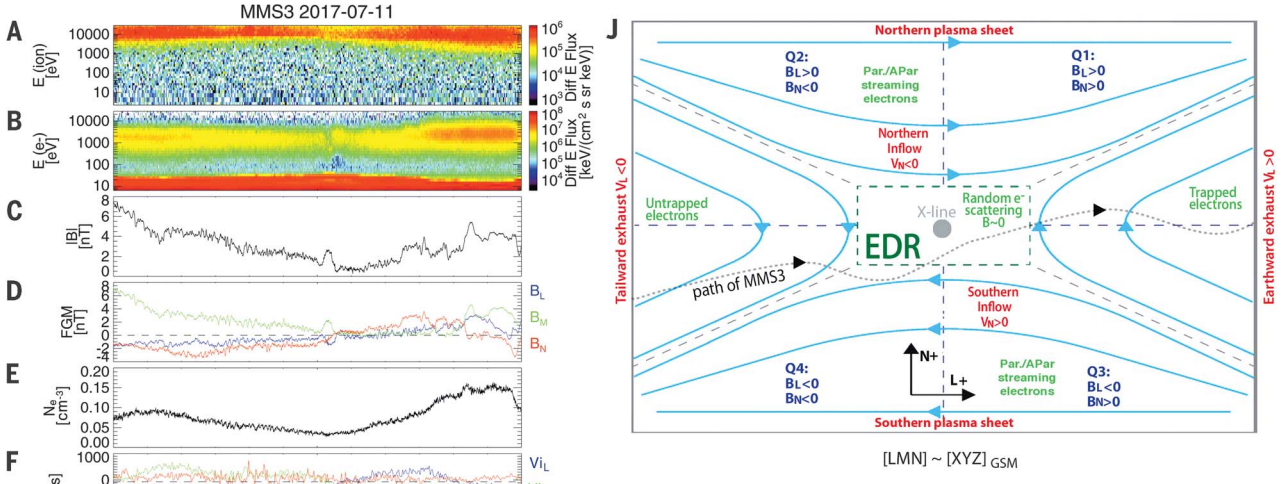

Fig. 1. MMS3 summary data near the crossing of the EDR at 22:34:03 on 11 July 2017. (**A** and **B**) Energy-time spectrograms of ion and electron energy flux, respectively. (**C**) Magnetic field magnitude. (**D**) Components in the *LMN* coordinate system, which is very close to the usual Geocentric Solar Magnetospheric (GSM) system (*10*). (**E**) Electron density. (**F**) Ion bulk velocity vector. (**G**) Electron bulk velocity vector. (**H**) The *L* component of ion and electron flow perpendicular to **B**, and of $\mathbf{E} \times \mathbf{B}/B^2$. (**I**) Electric field. (**J**) Illustration of a typical symmetric EDR in the *LMN* coordinate system, and the expected properties in various quadrants (Q1 to Q4), together with the inferred relative path of the MMS satellites as the X-line retreated tailward.

Figure 2, A to J, and Fig. 3, A to E, display data from one of the spacecraft, MMS3, in and around the EDR, again in *LMN* coordinates. Figure 2, K to N, shows reduced electron distribution functions (DFs) during the strong reconnecting current (J_M) at times before and during the peak of the quantity $\mathbf{J} \cdot \mathbf{E}'$ (where $\mathbf{E}' = \mathbf{E} + \mathbf{V}_e \times \mathbf{B}$), which is the electromagnetic energy conversion rate in the plasma frame, a signature of the EDR (*15*). Although $\mathbf{J} \cdot \mathbf{E}'$ is mostly positive throughout the period shown in Fig. 2, there are some regions with negative values, indicating that the electrons are transferring energy to the electromagnetic field, as seen also in simulations (*17*–*19*). Figure 3C shows that at all spacecraft, the signs of E_N and B_L were opposite, consistent with E_N converging toward the neutral sheet ($B_L = 0$) from both hemispheres, as expected for symmetric reconnection with a minimal guide field (*13*, *15*, *20*, *21*). MMS2 and MMS4 remained below the neutral sheet ($B_L < 0$ and $E_N > 0$) in the vicinity of the EDR crossing, whereas MMS1 and MMS3, located at higher *N*, made excursions above the sheet, where $B_L > 0$ and $E_N < 0$. This E_N field accelerates the neutral sheet electrons toward the inflow region, where they are accelerated along meandering trajectories (*22*) by the reconnection field, E_M ~ 1 to 2 mV/m (Fig. 3, C and E) (*10*). The electrons were eventually turned toward the *L*, or exhaust, direction by B_N as they exited the EDR, forming the electron jet seen in Figs. 2C and 3B on either side of the X-line.

The electron temperature profile in Fig. 2F shows strong anisotropy from 22:34:01.0 to 22:34:02.8 due to magnetic field–aligned electrons in the inflow region (*4*). During the EDR crossing, there was only a small rise (a few hundred eV) in parallel or perpendicular temperature (the parallel or perpendicular pressure divided by n_e), unlike the case of asymmetric reconnection (*3*), implying that a substantial fraction of the energy conversion went into the strong electron flows in the *M* and *L* directions.

The aspect ratio of the EDR is an approximate measure of the reconnection rate that has not been determined experimentally but has been studied theoretically and with simulations (*4*, *20*, *23*). Four-spacecraft timing analysis of the B_N reversal near 22:34:02.2 (see Fig. 2A) indicates that the X-line structure was moving tailward (V_{XL}, *L* component of the X-line velocity, ~ −170 km/s). The EDR length can be estimated by multiplying V_{XL} by the 1/e width of V_{eM} (~3 s; Fig. 2C), or by the $|V_{eL}|$ peak-to-peak time (~2 s; Fig. 2D), yielding a full length of 350 to 500 km (12 to 17 d_e). MMS also made a brief excursion into the EDR inflow region (beginning at ~22:34:01.0), indicated by the increase in $|B_L|$ and confirmed by the cooler electrons (Fig. 2B). By 22:34:02.2, the change in B_L and the timing analysis (V_{XN} ~ −70 km/s) show the structure moving southward, giving MMS also a normal motion into the EDR, reaching the neutral sheet and the peak of the cross-tail current by 22:34:03.0. Using Ampere's law (*10*), dividing the change in B_L during this normal motion into the EDR (Fig. 2A, ~22:34:02.0 to 22:34:03.0) by the average of J_M, yields a simple estimate of the normal half-width of 30 km, ~1 d_e (*10*). Thus, the aspect ratio is ~0.1 to 0.2, implying a reconnection rate consistent with fast reconnection (*24*).

Multiple crescent- and triangular-shaped features in the DFs (Fig. 2, K to N, and lower panels of Fig. 3) are the result of electron meandering motion in the electromagnetic field structure of the EDR. Figure 2L shows a DF taken at a location below (in *N*) the EDR, which features multiple crescents, seen as enhanced phase-space density at increasing velocities, similar to predictions (*25*–*27*) and shown in Fig. 2Q from the simulation of Fig. 2O (*10*). Contrary to magnetopause observations and models (*3*, *28*), we find more than one crescent. The observations show that crescents at higher $V_{\perp 1}$ are broader in $V_{\perp 2}$ than models predict; that is, particles with a larger range of $V_{\perp 2}$ bounce more than predicted by the model by a factor of 2. A likely explanation is that the current sheet electron distribution is more energetic than in the model, but the distributions may be sensitive to even a very small guide field (*29*). Models show that these crescents are generated by the interaction of bouncing

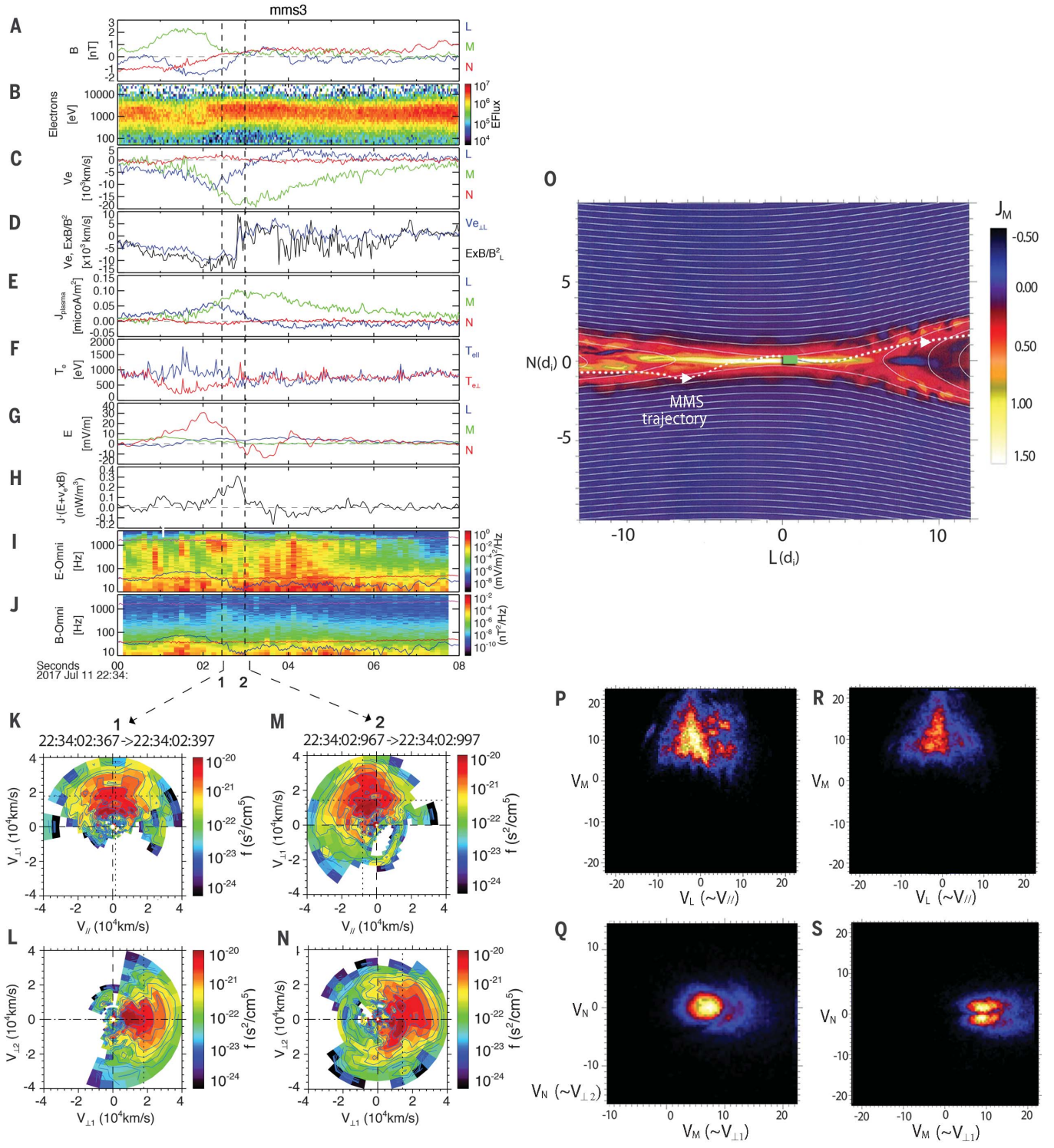

Fig. 2. MMS3 plasma and field data for the interval 22:34:00 to 22:34:08 on 11 July 2017. (**A**) Magnetic field components in *LMN* coordinate system. (**B**) Electron omnidirectional spectrogram, with minimum energy set at 50 eV to avoid the lower-energy spacecraft photoelectrons seen in Fig. 1B. (**C**) Electron bulk velocity. (**D**) *L* components of $\mathbf{V}_{e\perp}$ and $\mathbf{E} \times \mathbf{B}/B^2$. (**E**) Current from plasma measurements. (**F**) $T_{e||}$ and $T_{e\perp}$. (**G**) Electric field. (**H**) $\mathbf{J}\cdot\mathbf{E}'$. (**I** and **J**) Electric and magnetic omnidirectional frequency spectrograms, respectively, showing the power spectral density of electric and magnetic field fluctuations. (**K** to **N**) Electron velocity distribution functions at the times indicated. $V_{\perp 1}$ is $(\mathbf{b} \times \mathbf{v}) \times \mathbf{b}$, where **b** and **v** are unit vectors of **B** and $\mathbf{V}_e$; $V_{\perp 2} = \mathbf{v} \times \mathbf{b}$; and $V_{||}$ is the parallel electron velocity. $V_{\perp 1}$ is essentially the $\mathbf{E} \times \mathbf{B}$ direction, and the bulk flow component in that direction is indicated by the dashed vertical lines. (**O**) Magnetic configuration of a computer simulation (*10*, *31*), with color-coded reconnection current (J_M) and the inferred MMS trajectory overlain. (**P** to **S**) Reduced distribution f_e near the green box in (O) from that simulation, with velocity axes (in ion Alfvén speed units) corresponding to those of the data in (K) to (N). The color code is the same as in (O), but with simulation units representing phase-space density, like those of (K) to (N).

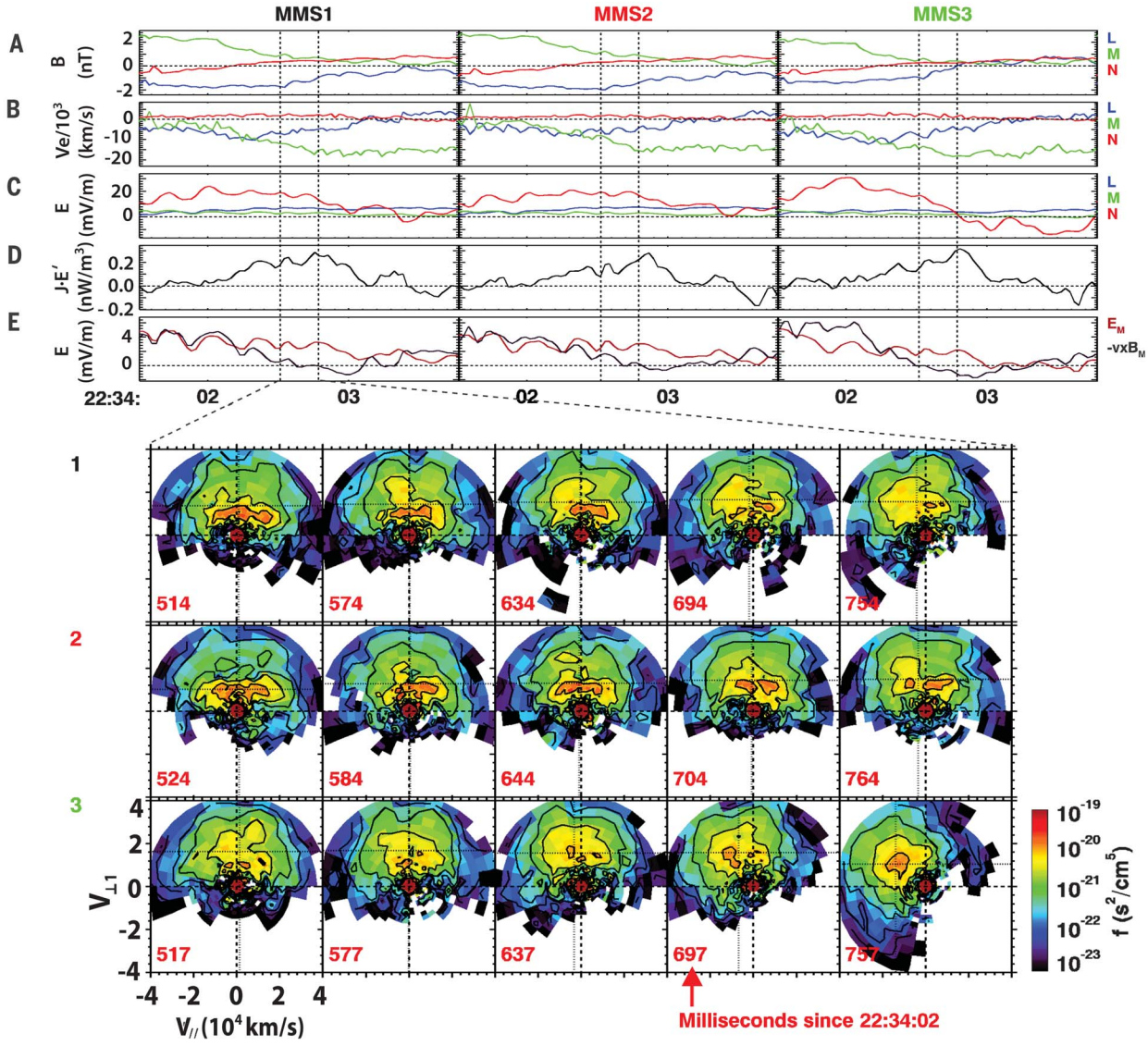

Fig. 3. Field data and electron DFs for three MMS spacecraft on 11 July 2017 for ~2 s around the EDR. Upper panels, for each spacecraft: (**A**) Components of **B**. (**B**) Electron bulk velocity. (**C**) **E**, where the reversal in E_N is seen on MMS3 and briefly MMS1, but not MMS2. (**D**) **J**·**E**′. (**E**) *M* component of **E** and −(**V**$_e$ × **B**). Lower panels from 2.604 s to 2.784 s are the reduced (summed over $V_{\perp 2}$) electron 30-ms DFs in ($V_{||}$, $V_{\perp 1}$) for each spacecraft at the times between the dotted lines in the upper panels.

electrons with both the normal (E_N) and the reconnection electric field (E_M), and their existence is consistent with canonical momentum conservation. The observation of multiple crescents indicates that the rather complex electron orbits are relatively unperturbed by high-frequency fluctuations in the electromagnetic fields. This implies that turbulent effects, which would scatter electrons and hence eliminate distinct phase-space features such as crescents, do not dominate the particle dynamics in the EDR.

Figure 2, M and N, displays a second DF, taken near the X point, which features a pronounced triangular shape in the plane containing *B*, broader at higher energies. Figure 2N shows two enhancements at lower $V_{\perp 1}$ (seen at $\pm V_{\perp 2}$, which is within ~20° of V_N) corresponding to inflowing populations from both above and below the X-line. These enhancements are similar to those that appear in the simulation shown in Fig. 2, O to S. In Fig. 2M, the triangular shape narrows in width as the energy increases, which also appears in the simulation (Fig. 2R). Bouncing electrons account for this feature: For each bounce, electrons gain successively more energy from acceleration by the reconnection electric field. If electrons have a finite V_L, they eventually interact with the magnetic field in the outflow and are ejected from the immediate vicinity of the X-line. The acceleration by the reconnection electric field and this ejection explain the triangular shape of the distribution: Only electrons with very small V_L remain near the X-line long enough to execute multiple bounces and be accelerated to higher energies.

The electron DFs of Fig. 3 (lower panels) show the evolution of the above features as MMS entered the EDR. From signatures of the inflow region (*4*), with DFs elongated along *B* (MMS1 and MMS2, first column, at 22:34:02.514), the spacecraft, with MMS3 leading, penetrated farther into the current layer and saw accelerated and gyrating electrons growing in energy as time (and *N* position) increased, showing a perpendicular crescent with energy >1 keV (2 × 10^4 km/s). By

22:34:02.724, all spacecraft were showing the perpendicular crescents, enhanced flow along the $\mathbf{E} \times \mathbf{B}$ direction, and also beaming features in the parallel directions. The parallel beams may be responsible for the high-frequency electrostatic noise near the upper hybrid frequency (~1200 Hz), seen at this time in Fig. 2I (*30*). When the spacecraft were fully within the reconnecting current layer (Fig. 2B, 22:34:02.694 to 22:34:02.757), there were higher-energy features rotating into both the $V_{\perp 1}$ (~M) and $V_{||}$ directions along with persistent counterstreaming, low-energy (~10,000 km/s) field-aligned beams. By 22:34:02.757, MMS3, which was deepest in the EDR, saw very energetic electrons in $V_{\perp 1}$ and also in the $-V_{||}$ direction; that is, these accelerated electrons were rapidly leaving the EDR region. The evolution of many such features can be seen in movie S1.

MMS observations of the magnetotail reconnection electron diffusion region show that it differs from that on the dayside because it involves symmetric inflow. The aspect ratio of the diffusion region (0.1 to 0.2), determined by MMS, is consistent with simulations of fast reconnection (*7*, *15*, *17*, *24*). MMS observations of electron dynamics in the diffusion region match predictions made by one class of theories and models: nearly laminar ones that assume that the effects of turbulence and associated fluctuations on the electron dynamics are small. Unlike the magnetopause results (*3*), we find that electrons can be accelerated up to three successive times by the reconnection electric field, possibly as a consequence of longer confinement in the symmetric magnetic structure. Taken together with MMS observations at the magnetopause, these results provide confirmation that reconnection is an efficient mechanism for the release of magnetic energy, for both geomagnetic substorms and auroral phenomena, and also discriminate between competing theories of reconnection. The energy width of the electron crescents differs from model predictions.

REFERENCES AND NOTES

1. T. Nagai *et al*., *J. Geophys. Res.* **103**, 4419–4440 (1998).
2. V. Angelopoulos *et al*., *Science* **321**, 931–935 (2008).
3. J. L. Burch *et al*., *Science* **352**, aaf2939 (2016).
4. L. J. Chen *et al*., *J. Geophys. Res.* **113**, 1–19 (2008).
5. T. I. Nagai *et al*., *J. Geophys. Res.* **116**, A04222 (2011).
6. M. Oka, T.-D. Phan, M. Øieroset, V. Angelopoulos, *J. Geophys. Res.* **21**, 1955–1968 (2016).
7. J. L. Burch, T. D. Phan, *Geophys. Res. Lett.* **43**, 8327–8338 (2016).
8. K. J. Genestreti *et al*., *J. Geophys. Res.* **122**, 11342–11353 (2017).
9. P. A. Cassak, M. A. Shay, *Phys. Plasmas* **14**, 102114 (2007).
10. See supplementary materials.
11. M. Øieroset, T. D. Phan, M. Fujimoto, R. P. Lin, R. P. Lepping, *Nature* **412**, 414–417 (2001).
12. A. Runov *et al*., *Geophys. Res. Lett.* **30**, 1579 (2003).
13. A. L. Borg *et al*., *Geophys. Res. Lett.* **32**, 32–35 (2005).
14. V. Angelopoulos *et al*., *Science* **321**, 931–935 (2008).
15. J. P. Eastwood, T. D. Phan, M. Øieroset, M. A. Shay, *J. Geophys. Res.* **115**, A08215 (2010).
16. D. N. Baker *et al*., *Geophys. Res. Lett.* **29**, 2190 (2002).
17. S. Zenitani, M. Hesse, A. Klimas, M. Kuznetsova, *Phys. Rev. Lett.* **106**, 195003 (2011).
18. M. A. Shay *et al*., *Geophys. Res. Lett.* **43**, 4145–4154 (2016).
19. P. A. Cassak *et al*., *J. Geophys. Res.* **122**, 11523–11542 (2017).
20. M. A. Shay, J. F. Drake, R. E. Denton, D. Biskamp, *J. Geophys. Res.* **103**, 9165–9176 (1998).
21. J. R. Wygant *et al*., *J. Geophys. Res.* **110**, A09206 (2005).
22. R. Horiuchi, T. Sato, *Phys. Plasmas* **1**, 3587–3597 (1994).
23. P. A. Sweet, in *Electromagnetic Phenomena in Cosmical Physics*, B. Lehnert, Ed. (Cambridge Univ. Press, 1958), pp. 123–134.
24. H. E. Petschek, *NASA Spec. Publ.* **50**, 425 (1964).
25. J. Ng, J. Egedal, A. Le, W. Daughton, L.-J. Chen, *Phys. Rev. Lett.* **106**, 065002 (2011).
26. N. Bessho, L.-J. Chen, J. R. Shuster, S. Wang, *Geophys. Res. Lett.* **41**, 8688–8695 (2014).
27. J. R. Shuster *et al*., *Geophys. Res. Lett.* **42**, 2586–2593 (2015).
28. M. Hesse, N. Aunai, D. Sibeck, J. Birn, *Geophys. Res. Lett.* **41**, 8673–8680 (2014).
29. J. Ng, J. Egedal, A. Le, W. Daughton, *Phys. Plasmas* **19**, 112108 (2012).
30. W. M. Farrell, M. D. Desch, K. W. Ogilvie, M. L. Kaiser, K. Goetz, *Geophys. Res. Lett.* **30**, 2259 (2003).
31. M. Hesse *et al*., *Phys. Plasmas* **25**, 032901 (2018).

ACKNOWLEDGMENTS

The dedicated efforts of the entire MMS team are greatly appreciated. We are especially grateful to the leadership of the GSFC project manager, the late Craig Tooley; the deputy project manager, B. Robertson, and the SwRI payload project manager, R. Black. **Funding:** Supported by NASA prime contract NNG04EB99C at SwRI; STFC(UK) grant ST/N000692/1; CNES, CNRS-INSIS, and CNRS-INSU in France; the Austrian Research Promotion Agency FFG; NASA grant NNX14AC78G at the University of Maryland; NASA grant NNX08A083G-MMS IDS at the University of California and the University of Delaware; and the Swedish National Space Board. **Author contributions:** Analysis and writing, R.B.T., J.L.B., T.D.P., M.H., and M.R.A.; analysis, J.S., R.E.E., L.A., R.N., K.J.G., D.L.T., S.W., L.-J.C., J.E.S., J.P.E., K.J.H., C.F., I.D., C.M., A.A., C.T.R., R.J.S., T.E.M., J.F.D., M.A.S., Y.V.K., M.O., A.N.J., and S.M.P.; electric field data, R.B.T., R.E.E., H.V., P.-A.L., Y.V.K., F.D.W., and N.A.; plasma data, D.J.G., W.R.P., B.L.G., C.J.P., L.-J.C., S.A.F., J.C.D., L.A.A., B.L., and Y.S.; magnetic field data, C.T.R., R.J.S., W.B., O.L.C., H.V., and R.B.T.; energetic particle data, D.L.T., I.C., B.H.M., D.N.B., J.F.F., J.B.B., and A.N.J. **Competing interests:** The authors declare that there are no competing interests. **Data and materials availability:** The MMS data are archived at https://lasp.colorado.edu/mms/sdc/public/. We used data from the period 22:29 to 22:37 UT on 11 July 2017, modified as described in (*10*).

SUPPLEMENTARY MATERIALS

www.sciencemag.org/content/362/6421/1391/suppl/DC1
Materials and Methods
Supplementary Text
Figs. S1 to S4
Movie S1
Reference (*32*)

12 February 2018; accepted 6 November 2018
Published online 15 November 2018
10.1126/science.aat2998

Science

Electron-scale dynamics of the diffusion region during symmetric magnetic reconnection in space

R. B. Torbert, J. L. Burch, T. D. Phan, M. Hesse, M. R. Argall, J. Shuster, R. E. Ergun, L. Alm, R. Nakamura, K. J. Genestreti, D. J. Gershman, W. R. Paterson, D. L. Turner, I. Cohen, B. L. Giles, C. J. Pollock, S. Wang, L.-J. Chen, J. E. Stawarz, J. P. Eastwood, K. J. Hwang, C. Farrugia, I. Dors, H. Vaith, C. Mouikis, A. Ardakani, B. H. Mauk, S. A. Fuselier, C. T. Russell, R. J. Strangeway, T. E. Moore, J. F. Drake, M. A. Shay, Yuri V. Khotyaintsev, P.-A. Lindqvist, W. Baumjohann, F. D. Wilder, N. Ahmadi, J. C. Dorelli, L. A. Avanov, M. Oka, D. N. Baker, J. F. Fennell, J. B. Blake, A. N. Jaynes, O. Le Contel, S. M. Petrinec, B. Lavraud and Y. Saito

Science **362** (6421), 1391-1395.
DOI: 10.1126/science.aat2998originally published online November 15, 2018

Reconnection in Earth's magnetotail

Magnetic fields in plasmas can rapidly rearrange themselves in a process known as magnetic reconnection, which releases energy and accelerates particles. Torbert *et al.* used the Magnetospheric Multiscale (MMS) mission to probe a reconnection event in Earth's magnetotail—the region of plasma downstream from the planet as it moves through the solar wind. MMS has previously studied reconnection in the upstream magnetopause, but a different orbit was used to study the magnetotail, where the symmetry of the process is different. The authors measured plasma properties on scales of the electron dynamics, leading to insights that will apply in other regions where magnetic reconnection occurs.
Science, this issue p. 1391